JACS
JOURNAL OF THE AMERICAN CHEMICAL SOCIETY
pubs.acs.org/JACS
Article

NMR-Based Measurements of Site-Specific Electrostatic Potentials of Histone Tails in Nucleosome Core Particles

Nicolas Bolik-Coulon,* Philip Rößler, and Lewis E. Kay*

Cite This: J. Am. Chem. Soc. 2025, 147, 14519−14529
Read Online
ACCESS | Metrics & More | Article Recommendations | Supporting Information

ABSTRACT: Electrostatics play a dominant role in guiding many biological processes. This is especially the case in the context of chromatin, where charge interactions modulate diverse activities such as DNA repair, transcription, replication, condensation, and phase separation. Using NMR experiments quantifying solvent paramagnetic relaxation enhancements of backbone amide and side chain methyl protons in the presence of paramagnetic cosolutes and focusing on the nucleosome core particle (NCP), we report near surface electrostatic potentials of tail residues of each of the four histone components of the NCP. These are all negative, despite sequences comprising a high density of positively charged amino acids, emphasizing the strong contribution of the negatively charged DNA with which the tails interact. Changes in electrostatic potentials of as much as 60 mV between isolated histone tails and tails in the context of the NCP are calculated. Notably, the tail potentials can vary significantly from each other, with enrichment in glycine residues correlating with less negative values, highlighting differences in the interactions with DNA.

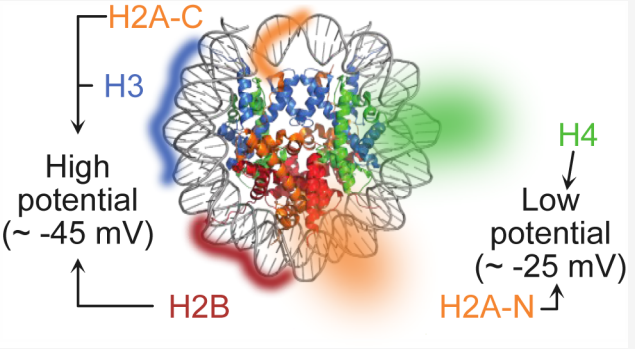

INTRODUCTION

Intrinsically disordered regions (IDRs) of proteins and protein complexes play critical roles in driving biomolecular function.[1] This is particularly the case in the context of chromatin, made up of basic building blocks called nucleosome core particles (NCPs), with each NCP comprised of two copies each of four histones, H2A, H2B, H3, and H4.[2,3] Canonical histones share a common structural organization, with unstructured N-terminal regions of between approximately 10 (H2A) to 35 residues (H3), as well as a small IDR at the C-terminus of H2A, and structured domains forming the core of the octamer around which 147 base pairs of DNA are wrapped,[2] Figure 1a. As might be expected, the negatively charged DNA and the positively charged histone components of NCPs give rise to a highly charged structure.[4] For example, each NCP has a net charge of approximately −150e (+144e from the 8 histones and −294e due to the 147 base pairs of DNA for the system under study here, where e is the elementary charge equal to 1.6 × 10^{-19} C), and ion counting experiments have shown that the electric fields associated with the NCP are stronger than the equivalent naked linear DNA molecule due to the cylindrical shape of the particle,[4] containing approximately 1.7 turns of left-handed super helical DNA.

The high charge density of the NCP particle, and by extension of chromatin, challenges the packaging of the approximately 2 m of human DNA into a nucleus of diameter 5−10 μm.[5] An advantage, however, is that the charge can be exploited by the cell to regulate both chromatin structure and function,[6,7] with post-translational modifications to the lysine- and arginine-rich histone tails playing a prominent role in this regard. An example is provided by acetylation which neutralizes the otherwise positively charged lysine tail residues[8] or by poly-ADP ribosylation of serine residues on H2B and H3 tails,[9−12] both of which signal sites of DNA damage and disrupt interactions between the affected tails and DNA, decreasing DNA packing and increasing accessibility to effector proteins.[13,14]

Despite the importance of histone tails in regulating both DNA packing and interactions with other proteins that control DNA damage repair, replication, and transcription, and the role(s) that tail charges and post-translational modifications play in these processes,[15] experimental measures of histone tail electrostatics are notably lacking. One of the limiting factors reflects the intrinsically disordered nature of the tails, which complicates structural studies via X-ray crystallography and cryo-electron microscopy. Indeed, chain density is lacking for most of the tail residues in X-ray or cryo-EM derived models, challenging the calculation of tail electrostatic potentials using

Received: January 24, 2025
Revised: March 26, 2025
Accepted: April 3, 2025
Published: April 16, 2025

https://doi.org/10.1021/jacs.5c01567
J. Am. Chem. Soc. 2025, 147, 14519−14529

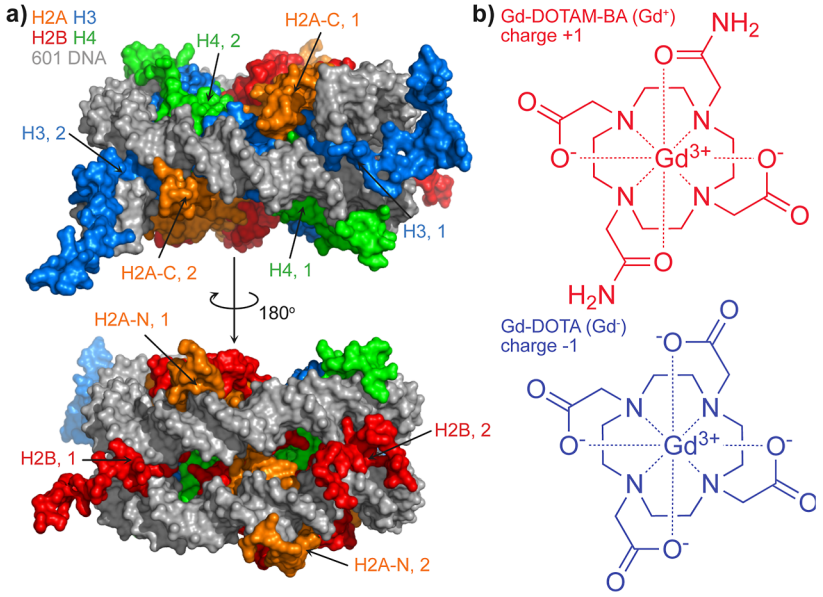

Figure 1. Structures of the molecules used in this study. (a) Views of the *Xenopus laevis* NCP wrapped with human α-satellite DNA (PDB 1KX5),[77] with each histone color-coded, as indicated, and the exit point of each tail shown with an arrow. Histone H2A tails are indicated as H2A-N (N-terminal tail) and H2A-C (C-terminal tail); all other tails are N-terminal. Each histone is present in two copies (for example, H2B, 1 and H2B, 2). The NCP used in this study is structurally very similar to the one in the figure; however, the histones are from *Drosophila melanogaster* and the DNA is the Widom 601 sequence.[66] The *Xenopus laevis* NCP is highlighted, as more of the tail sequences are shown in this structure. (b) Cosolutes used to measure sPRE rates. The negative cosolute is a complex of gadolinium with a DOTA cage (bottom), while the positive cosolute (top) involves a variant of DOTA where two opposite carboxyl groups are replaced by amide moieties.

Poisson−Boltzmann methods, as this approach requires structures of the molecule of interest.[16] In contrast, solution NMR is ideally suited to study the dynamic histone tails, as motion averages out spin interactions that would otherwise result in broad and low intensity peaks in the spectra. As a result, a significant number of NMR studies have focused on the dynamics of NCP tails either without or with modifications using straightforward $^{1}H-^{15}N$ correlation spectroscopy,[17−28] and detailed, atomic resolution descriptions of motion over a wide time-scale window are now available.[17−19,21,23,27−29]

Insights into the important roles of electrostatics in biomolecular function have been obtained through NMR measurements of pK_a values of pH titratable moieties, and numerous studies along these lines have been performed.[30,31] This includes recent work in which residue-specific pK_a values for Glu, Asp, and His side chains comprising the acidic patch of an isolated H2A−H2B histone dimer construct were measured at physiological pH.[32] Important advances in biomolecular NMR methods using paramagnetic relaxation enhancement (PRE) cosolutes, most notably by Iwahara and co-workers,[33,34] and Okuno and Clore,[35,36] have led to the establishment of a robust experimental approach for the measurement of per-residue near surface electrostatic potentials, ϕ_{ENS}, for biological molecules.[37,38] Experiments quantify solvent PREs (sPREs) of ^{1}H spins of the macromolecule of interest through measurements using at least a pair of paramagnetic cosolutes having similar structures but different charges. The sPREs so obtained can then be used to directly calculate ϕ_{ENS} values (see below). Applications involving either proteins or nucleic acids, or in some cases both, have appeared.[33,36,39−43] Notably, this methodology is equally applicable to folded and unfolded biomolecules, and structures (folded) or structural ensembles (unfolded) are not required, in contrast to calculations of electrostatic potentials using Poisson−Boltzmann based programs such as APBS[44,45] or DelPhi.[46,47] Thus, the NMR experiments are particularly powerful for obtaining per-residue measures of ϕ_{ENS} values of IDRs, such as the 103 residue C-terminal region of the RNA binding stress-granule protein CAPRIN1,[48,49] whose electrostatic potentials were measured during its phase separation trajectory.[41,50] Building on this work, we report here ϕ_{ENS} values of histone tail residues of the 200 kDa NCP, based on sPRE measurements of both backbone amide and Ile (δ1), Leu, and Val side chain methyl group protons. Notably, even though the net charge of each tail in isolation is positive, we find that in the context of the NCP, their per-residue ϕ_{ENS} values are all negative, with the N-terminal H2A (H2A-N) and H4 tails having distinctly less negative electrostatic potentials than the other tails. Our study provides a picture of histone tail-DNA interactions and structural dynamics and suggests an important role for glycine residues in modulating tail electrostatics.

METHODS

Histone/601 DNA Expression, Purification, and Formation of the NCPs. A detailed description has been given previously.[17,51]

NMR Spectroscopy. The NCP solution was split to form three samples: (1) the diamagnetic reference sample that does not contain cosolute, (2) a Gd^{+} sample, containing Gd-tetraazacyclododecane-bisacetate-bisacetamide (Gd-DOTAM-BA; Macrocyclics, Inc.) cages at a concentration of approximately 0.1 mM, and (3) a Gd^{-} sample, with Gd-tetraazacyclododecane-tetraacetate (Gd-DOTA; Macrocyclics, Inc.) cages at a concentration of approximately 2 mM. D_2O was added to each NCP sample to a final concentration of 5%. After initial measurements were performed (i.e., at the indicated cosolute concentrations), increasing amounts of cosolutes were added to reach final concentrations of 0.2 and 0.3 mM for Gd-DOTAM-BA, and 4 and 6 mM for Gd-DOTA so that further experiments could be carried out. We have found that accurate amounts of cosolute could be added using a procedure by which 2−6 μL of a stock solution of

https://doi.org/10.1021/jacs.5c01567
J. Am. Chem. Soc. 2025, 147, 14519−14529

Table 1[a]

	NCP, dia	NCP, Gd^+	NCP, Gd^-	Ref, Gd^+	Ref, Gd^-
NCP (135 μM)	207	207	207	-	-
NMR buffer	125.5	123.1	119.4	207 + 123.1	207 + 119.4
Gd cage	-	2.38	6.14	2.38	6.14
D_2O (pure)	17.5	17.5	17.5	-	-
DSS (20 mM)	-	-	-	17.5	17.5

[a]Volumes used to prepare samples are indicated in 1 μL units. Stock concentrations are indicated for the NCP and DSS, both dissolved in NMR buffer, while the stock concentrations of the Gd-DOTAM-BA and Gd-DOTA cosolutes were 14.68 and 114 mM, respectively. Ref, $Gd^{\pm}$ refers to the reference samples "mimicking" the NCP samples where the 207 μL of NCP was replaced by 207 μL of buffer. Note that the NMR buffer was pipetted twice (once with 207 μL and then with the indicated amount, for example, 123.1 or 119.4 μL) to closely mimic the preparation of the NCP samples. The samples indicated in the panel were generated in 5 mm NMR tubes; additional solutions for 3 mm inserts, used for the Evans method, were prepared as described above; only in the 3 mm inserts was D_2O added.

the appropriate compound was transferred to a clean Eppendorf tube, forming a drop in the tube that is held together by surface tension and subsequently transferring this drop into an NMR shigemi tube containing the NCP sample using a glass pipet. The accuracy of this transfer method was verified by measuring water T_1 sPREs (detailed below).

NMR experiments were performed either on a 11.7 T (500 MHz ^{1}H frequency) Bruker AVANCE III HD spectrometer (measurement of water T_1 values) equipped with a liquid nitrogen-cooled z pulsed-field gradient triple-resonance probe or on a 23.5 T (1 GHz ^{1}H frequency) Bruker AVANCE NEO spectrometer equipped with a cryogenically cooled *x,y,z* pulsed-field gradient triple-resonance probe (measurement of NCP sPREs). All spectra were processed using *NMRPipe*[52] and visualized in *Sparky*.[53]

Water ^{1}H R_1 rates (for estimation of cosolute concentrations, see "Determination of Cosolute Concentrations", below) were measured at 11.7 T, 25 °C, using a saturation-recovery scheme (relaxation recovery for a duration t), as described previously.[41] The intensity of the water signal, $I(t)$, was extracted by sum integration of the recorded 1D data sets and the water relaxation rate (and thermal equilibrium intensity I_{eq}) obtained by fitting the evolution of the intensity to the relation, $I(t) = I_{eq}(1 - e^{-R_1 t})$, where $R_1 = 1/T_1$.

Amide proton R_2 relaxation rates were measured at 23.5 T, 37 °C, using a gradient enhanced [^{1}H−^{15}N]-HSQC pulse scheme with a ^{1}H spin−echo variable delay (−τ−selective 180°−τ−) inserted immediately prior to acquisition.[54] In applications involving protonated samples, homonuclear *J*-coupled evolution involving $^1H^N$ and aliphatic proton spins is refocused using a 2 ms selective REBURP ^{1}H 180° pulse[55] (centered at 8.7 ppm, refocusing bandwidth of ±0.8 ppm at 1 GHz) applied in the center of the ^{1}H spin−echo. As the sample used in this study is perdeuterated this is not a concern here, however, the amide selective REBURP pulse ensures that the water signal is not perturbed, an important consideration for obtaining high quality data. A pair of composite $(90_x240_y90_x)$[56] ^{15}N pulses was inserted at $\tau/2$ in each half of the spin−echo to refocus ^{1}H−^{15}N dipole/^{1}H−CSA cross-correlated spin relaxation during the echo element, as described previously.[54] The following relaxation delays were used: 2.5, 5, 7, 10, 15, 20, 25, and 30 ms. Methyl ^{1}H transverse sPREs were quantified (37 °C) by measuring the decay of the slow component of proton magnetization using an HMQC-derived pulse scheme described previously[57] except that composite $(90_x240_y90_x)$ ^{13}C pulses replaced the pair of 180° pulses to refocus ^{1}H−^{13}C dipole/^{1}H−CSA cross-correlated spin relaxation during the echo. A WATERGATE block[58] was inserted as the refocusing pulse in the middle of the ^{1}H spin−echo to dephase the water signal. The following relaxation delays were used: 10, 30, 50, 70, 90, and 110 ms.

Intensities were extracted from all relaxation data sets using the *Peakipy* software package (https://j-brady.github.io/peakipy/), and relaxation rates (and initial intensities, I_0) were obtained by fitting the time-evolution of the intensity to the exponential decay function $I(t) = I_0 e^{-R_2 t}$, where t is the relaxation delay. Errors in the extracted relaxation rates were estimated as the standard deviation in R_2 from 100 bootstrap cycles.[59]

Determination of Cosolute Concentrations. Accurate values of near-surface electrostatic potentials require that measured sPRE rates be normalized to the concentrations of the cosolutes used in the experiments.[60] To obtain accurate concentrations of the Gd-based cosolutes, we used the Evans method, which takes advantage of the difference in magnetic susceptibilities between a sample with and without gadolinium.[61,62] Starting from stock solutions of Gd-DOTAM-BA (14.68 mM) and Gd-DOTA (114 mM), we prepared two reference samples (with desired concentration values of 0.1 and 2 mM for the Gd^+ and Gd^- compounds, respectively; no NCP), exactly as we would prepare NCP samples, except that the solution of NCP that would be added was replaced with NMR buffer and, similarly, the D_2O that would have been added to the NCP sample for lock was substituted by a solution of 20 mM 2,2-dimethyl-2-sulfonate (DSS). Note that the same pipettes were used for reference and NCP samples. An additional sample containing 1 mM DSS in an NMR buffer with 5% D_2O (no cosolute added) was placed in a 3 mm NMR tube; all other samples were in 5 mm NMR tubes. The gadolinium concentration in the two reference samples was obtained by placing the inset tube (3 mm) into the 5 mm tube and measuring the chemical shift difference of the DSS between the inner and outer tubes from which [Gd] is calculated according to[60]

$$[\mathrm{Gd}] = 3.05 \times 10^{-5} \times T \times \Delta \quad (1)$$

where T is the absolute temperature (298.15 K) and Δ is the chemical shift difference (ppm). A pair of duplicate samples for each cosolute was prepared to measure the concentrations of gadolinium in the reference samples, assumed to be equal to the concentrations in the NCP samples. Values of 0.11 mM for Gd-DOTAM-BA and 1.95 mM for Gd-DOTA were obtained, within a few percent of the expected concentrations; in the text, we refer to the concentrations as 0.1 and 2 mM, for simplicity. Table 1 below details the pipetted volumes and compositions of each sample.

In order to carry out measurements at higher concentrations of cosolutes, and starting from the initial NCP samples with 0.1 and 2 mM of the Gd-compounds, the appropriate aliquots of the stock Gd solutions were added (see "NMR Spectroscopy" above). To establish the new concentrations of cosolutes, the water longitudinal sPRE rates, Γ_1, were measured at 11.7 T, making use of the linear relationship between the sPRE and the concentration of paramagnetic compound

$$\Gamma_1(c) = \alpha \times c \quad (2)$$

where α is a constant and c is the cosolute concentration. Thus, the concentration of cosolute in any sample can be determined by

$$c = \frac{\Gamma_1 c^{\circ}}{\Gamma_1^{\circ}} \quad (3)$$

where Γ_1° is the water sPRE rate for a cosolute concentration of c° (in this case the initial cosolute concentrations of 0.11 and 1.95 mM for the + and − charged compounds, respectively). The extracted PRE rates for a given concentration of cosolute, c, are normalized by dividing by c before calculating ϕ_{ENS}, as discussed below. Errors in

https://doi.org/10.1021/jacs.5c01567
J. Am. Chem. Soc. 2025, 147, 14519−14529

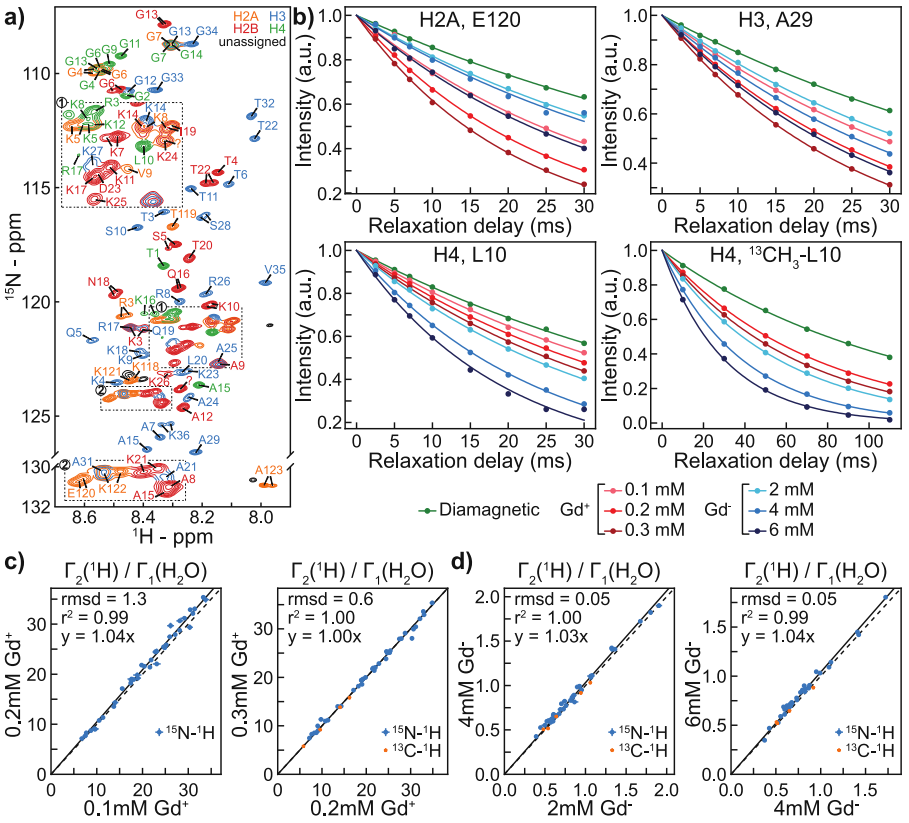

Figure 2. Measurement of sPRE rates of tail amide and methyl probes in NCP samples. (a) [^{1}H−^{15}N]-HSQC spectrum of a [^{2}H−^{15}N]-ILV NCP sample recorded at 1 GHz, 37 °C. Each peak is color-coded to indicate the histone from which it originates, using the same color-coding as in Figure 1a. Note that the high molecular weight of the NCP (200 kDa) leads to broadening of the core peaks such that only the tail residues are visible. Partially overlapping peaks derived from different histones are colored with multiple colors. Crowded regions of the spectrum are shown in insets 1 and 2; the symbol "?" indicates an unassigned peak. (b) Representative relaxation decays of amide or methyl ^{1}H magnetization for three histone tail residues, color coded according to whether the sample is diamagnetic (green, no cosolute) or includes Gd^{+} (shades of red) or Gd^{-} (shades of blue) cosolutes of various concentrations. Fits of the decays to exponential decay functions are shown with the solid lines. (c,d) Correlation of NCP sPRE rates normalized by the water longitudinal sPRE rate (referred to as α in the text) for different concentrations of Gd^{+} (c) and Gd^{-} (d) compounds.

ϕ_{ENS} are obtained by propagating errors in measured PRE rates with residues with errors higher than 3 mV discarded.

Calculation of ϕ_{PB}. Near surface electrostatic potentials were computed (ϕ_{PB}) for isolated histone tails generated with extended conformations using the APBS program.[44,45] As the potentials of the isolated tails are to be compared with the corresponding tails in the context of the NCP, it is important that terminal charge that would be present in the isolated tails, but not in the NCP, be eliminated. To this end, the structures of the isolated tails were built in PyMOL,[63] with five extra glycine residues added to their C-termini (or to the N-terminus of the C-terminal H2A tail, H2A-C) to remove the effect of the terminal carboxyl group (or amino group for H2A-C). APBS was run after converting the pdb format into the pqr format to produce the desired Poisson−Boltzmann (PB) potentials, ϕ_{PB}, using a setup given in Supporting Information

$$\phi_{PB} = -\frac{k_B T}{2e}\ln\left(\sum_{i=1}^{N}\rho_i r_i^{-6} e^{-e\phi_i/k_B T} \Big/ \sum_{i=1}^{N}\rho_i r_i^{-6} e^{e\phi_i/k_B T}\right) \quad (4)$$

In eq 4, k_B is Boltzmann's constant, T is the absolute temperature, e is the elementary charge, ϕ_i is the potential calculated from APBS at grid point i, r_i is the distance between grid point i and the ^{1}H nucleus in question, and ρ_i is set to 1 or 0 depending on whether the grid point is accessible (1) to the cosolute or not (0); further details are provided elsewhere.[60]

RESULTS

Measurement of ϕ_{ENS} Values in Highly Charged Systems. As discussed in detail previously, ϕ_{ENS} values are calculated from site-specific sPRE rates measured using structurally similar cosolutes that differ in charge[33,37,38]

$$\phi_{ENS} = \frac{-k_B T}{(q_i - q_j)e}\ln\left(\frac{\Gamma_{2,i}}{\Gamma_{2,j}}\right) \quad (5)$$

In eq 5, q_i and q_j are the net charges of the two cosolutes (in the case here where +1 and −1 charged cosolutes are used, Figure 1b, $q_i = q_+ = 1$, $q_j = q_- = -1$), k_B is Boltzmann's constant, T is the absolute temperature, and $\Gamma_{2,i} = \Gamma_{2,+}$ and $\Gamma_{2,j} = \Gamma_{2,-}$ are the measured sPRE values, calculated as the difference in ^{1}H transverse relaxation rates, R_2, in the presence and absence of cosolute (i.e., $\Gamma_{2,k} = R_2(q_k) - R_2(\text{no cosolute})$), and normalized for the differences in concentration between positive and negative cosolutes (see Methods). Measurements of ϕ_{ENS} values for histone tails of the NCP are challenged by the high negative charge of the nucleosome so that $\Gamma_{2,-}$ values tend to be small. In the case where positive and negative PROXYL or TEMPO cosolute pairs are used to obtain ϕ_{ENS}, as is often done,[33−36,38,40−43,50] this difficulty is exacerbated by the fact that these compounds have only a single unpaired electron ($S = 1/2$, where S is the electron spin quantum

https://doi.org/10.1021/jacs.5c01567
J. Am. Chem. Soc. 2025, 147, 14519−14529

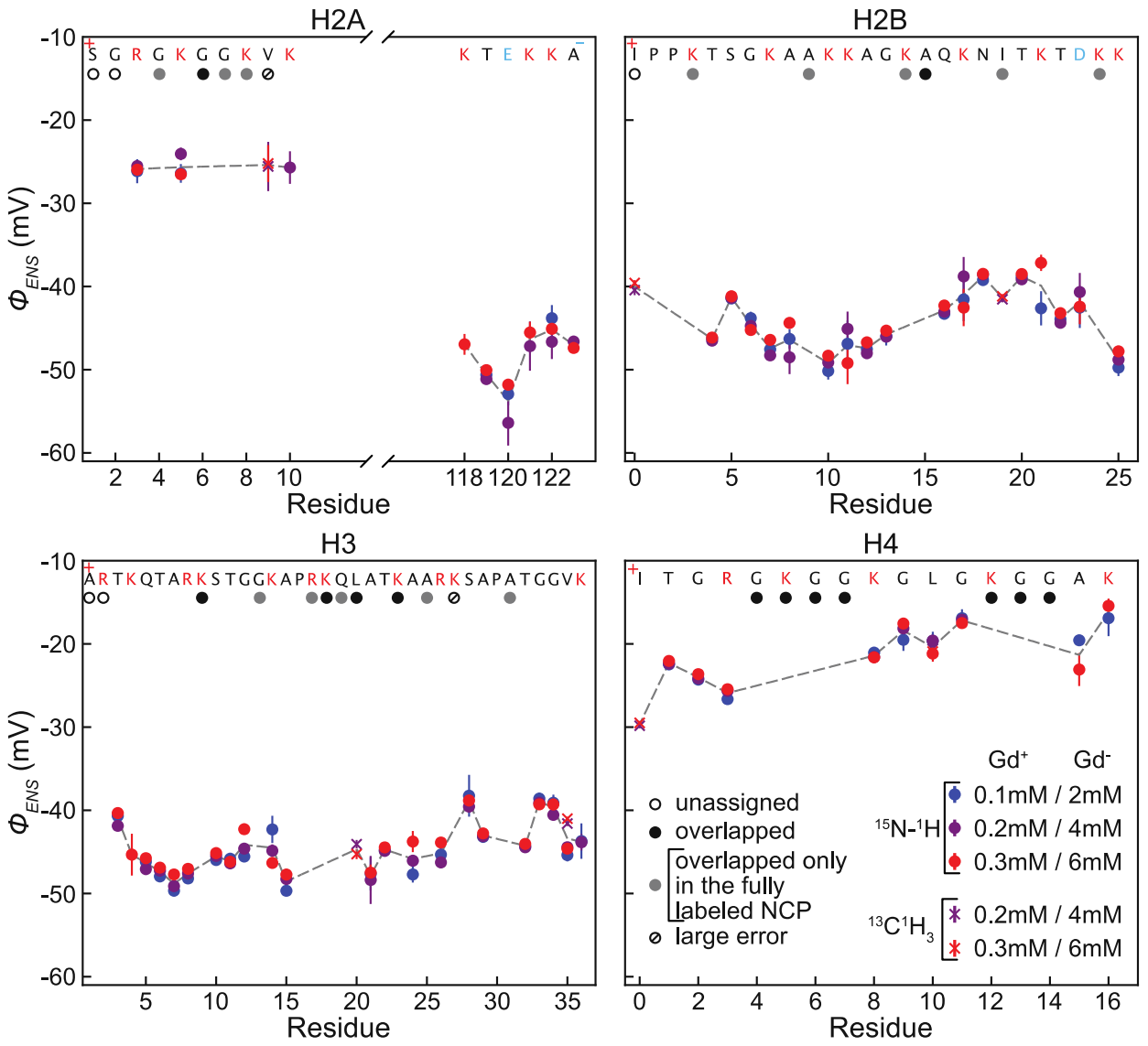

Figure 3. ϕ_{ENS} values for amide and methyl ^{1}H probes in histone tails for each histone, calculated using sPRE rates measured with different pairs of cosolute concentrations (eq [5]): 0.1 mM (Gd^{+}) and 2 mM (Gd^{-}), 0.2 mM (Gd^{+}) and 4 mM (Gd^{-}), and 0.3 mM (Gd^{+}) and 6 mM (Gd^{-}). Potentials obtained from relaxation measurements of methyl ^{1}Hs are shown with crosses. Only average ϕ_{ENS} values are shown for isopropyl methyl groups, with variations of less than 1 mV for the (δ1, δ2) pairs of L10 of H4, and 5 mV for L20 of H3. The amino acid sequence of each tail is indicated in the appropriate panel (top), with basic amino acids (K and R) shown in red and acidic amino acids (D and E) in blue, along with + and − to indicate the charge of each terminus. Note that the sequences listed can differ very slightly from the canonical Uniport sequences (Figure S4, Table S1) due to cloning artifacts or from the addition of an N-terminal Ile to improve expression. Tail boundaries are defined on the basis of whether backbone amides can be observed in [^{1}H−^{15}N]-HSQC spectra. The N-terminal residue for each of the (H2A-N, H3, and H4) tails (Met) or H2B tail (Gly) is not listed as crosspeaks from it are not observed in NMR spectra. In the case of H2B, a GM initial sequence is present. Charge and fractional Gly content in the text are calculated with all terminal residues included. Probes from residues whose ϕ_{ENS} value could not be measured in amide spectra are denoted with circles (placed immediately underneath the one-letter code): unassigned (empty), overlapped (black and gray), or large error in the potentials (i.e., higher than 3 mV, circled line). Residues whose crosspeaks are overlapped only in amide spectra of the fully labeled [^{2}H−^{15}N]-ILV NCP, but not in amide spectra of NCPs, where histones are labeled individually are denoted with the gray circles. All tail methyl correlations are resolved in [^{1}H−^{13}C]-spectra. The dashed gray line connects the average potential of each residue for visual clarity.

number) and hence only a limited sPRE effect. Iwahara and coworkers have recently suggested using Gd-based cosolutes (Figure 1b), for which all seven Gd 4f electrons are unpaired (S = 7/2).[60] This gives rise to much larger sPREs at a fixed concentration of cosolute, with increased relaxivities over the corresponding nitroxide compounds by as much as 20−30 fold. In the NCP studies reported here, the use of the Gd-compounds is critical. It is noteworthy that we have used the Gd^{+}/Gd^{-} pair of cosolutes, even though the NCP is highly negatively charged. Although it might appear that the neutral cosolute would be more effective than the negatively charged compound, we have experienced difficulties obtaining robust measures of ϕ_{ENS} when one cosolute of the pair is neutral and prefer, therefore, to use the ± pair of compounds for which there is extensive validation in the literature[60,64] (see, for example, Figure S7D−F of Yu et al.[60] highlighting some of the issues with neutral cosolutes).

ϕ_{ENS} Values of NCP Tail Residues. In some of our previous NCP studies, we had prepared a series of samples where one of each of the four histone-types was labeled with

https://doi.org/10.1021/jacs.5c01567
J. Am. Chem. Soc. 2025, 147, 14519−14529

NMR active spins, while the remaining histones were perdeuterated (i.e., NMR silent).[17,18] However, at least a pair of samples of a given type is required for each ϕ_{ENS} measurement (positive and negative cosolute; relaxation data can be recorded on the diamagnetic sample prior to the addition of the cosolute), necessitating the preparation of eight samples in the present case. We decided, therefore, to generate NCP samples where all four histones were ^{2}H, ^{15}N, and $^{13}CH_3$ labeled at Ile ($\delta1$), Leu, and Val methyl positions (only one of the isopropyl methyl groups of Leu and Val was labeled, in a nonstereospecific manner,[65] referred to as [$^{2}H-^{15}N$]-ILV labeling in the text that follows). Figure 2a shows the [$^{1}H-^{15}N$]-HSQC spectrum of an NCP sample prepared with histones from *Drosophila melanogaster* wrapped with the Widom 601 DNA sequence,[66] with each peak color-coded to delineate from which histone it derives, using the conventional coloring scheme for histones,[2] as in Figure 1a. Because of the size of the NCP (200 kDa), only $^{1}H-^{15}N$ correlations from tail residues are observed in NMR spectra, with the core of the particle amenable to study via methyl group probes[17,18,22,24,51,67,68] that benefit from a methyl-TROSY effect.[69] Although a factor of 4 in measurement time is saved by acquiring data on all histones simultaneously, a potential drawback arises from the overlap of peaks derived from the different histones. This problem can be mitigated to a certain extent by using highly deuterated samples, ensuring that line widths of crosspeaks in $^{1}H-^{15}N$ correlation maps are minimized, thereby improving resolution. Deuteration also allows ϕ_{ENS} values of tail residues close to the structured NCP regions to be quantified by decreasing relaxation losses that would otherwise be severely limiting in the context of protonated samples. Our study further benefits from measurements at a static magnetic field of 23.5 T, corresponding to a ^{1}H resonance frequency of 1 GHz. The net result is that three, five, and seven amides are not available for analysis in the N-terminal H2A tail, the H2B tail, and the H3 tail, respectively, which could otherwise be quantified using separately labeled samples, a modest price to pay for savings in both measurement time and sample costs. In total, 3/10, 6/6, 17/25, 22/34, 9/17 of the NMR observable amides in H2A-N, H2A-C, H2B, H3, H4 tails were analyzed in the present study. Electrostatic potentials for all ILV methyl groups were obtained; however, there are few such residues in the tails, and the present work, therefore, focuses primarily on amide backbone protons for estimating ϕ_{ENS} values.

Figure 2b illustrates the intensity profile decays as a function of relaxation time for several probes from different histones. In addition to the "diamagnetic" relaxation data (green; in this case measured in the absence of cosolute), profiles with both positive and negative charged cosolutes were recorded at different concentrations, Figure 2b. It is notable that the relative effects of the different cosolutes and their concentrations on decay curves can vary from site to site. For example, while the diamagnetic rate profiles decay most slowly for all four probes highlighted, as expected, for E120 and A29 of H2A and H3, respectively, the 0.3 mM Gd^{+} cosolute results in the fastest decay (dark red profiles). In contrast, for both the amide and $\delta2$-methyl probes of L10 from H4, the sPRE rates are larger for the 6 mM Gd^{-} cosolute than for the Gd^{+} compound at 0.3 mM (faster decay rates). Even without further analyses, these results suggest that the electrostatic potentials for the different tails are distinct with a smaller negative potential for the H4 tail in relation to the C-terminal tail of H2A and the tail of H3.

In any sPRE study, there is always the possibility of unwanted binding of the cosolute to pockets in the biomolecule of interest, leading to elevated sPRE rates and erroneous interpretation of the data. This might particularly be the case in studies of highly charged molecules, such as the NCP, where it is easy to envision that the Gd^{+} compound could bind preferentially to specific regions of the DNA. With $\Gamma_{2,i}$ values available for many sites, determined using different cosolute concentrations, it is now possible to evaluate whether some of the PRE rates reflect, at least partially, untoward binding of cosolutes. Figure 2c shows linear correlation plots of $\Gamma_{2,i}$ rates measured at different cosolute concentrations and normalized against longitudinal PRE rates measured for water in the NCP sample, $\alpha = \frac{\Gamma_2(NCP)}{\Gamma_1(H_2O)}$ (i.e., effectively normalized for concentration of cosolute). As α values are expected to be independent of the cosolute concentration in the absence of binding, a $y = x$ linear correlation of α ratios at different concentrations provides strong evidence that site-specific interactions, if present at all, are minimal. In contrast, if specific binding occurs, then Γ_2(NCP) values will increase rapidly with cosolute concentration for those probes proximal to the binding site until a 'saturation' point is reached and subsequently increase more gradually. Thus, the resulting α values will decrease with increasing cosolute concentration. Our concentration-dependent relaxation data, showing good agreement between α values recorded at different cosolute concentrations (Figure 2c), are consistent, therefore, with an absence of specific cosolute—NCP interactions. This is further substantiated by comparing $^{1}H-^{15}N$ spectra recorded with and without cosolutes. The lack of chemical shift perturbations in such a comparison indicates that specific binding to the NCP does not occur, as observed in Figure S1, where spectra recorded for ± Gd-DOTAM-BA at a concentration of 0.3 mM (highest concentration of positive cosolute used in this study) are overlaid. Note, as described above, the concentrations of Gd-based cosolutes are significantly less than the amounts of PROXYL-derivatives needed to achieve the same level of sPREs,[60] minimizing the likelihood of binding in the first place.

Figure 3 plots ϕ_{ENS} values as a function of tail residue for each histone, recorded on NCP samples at concentrations of approximately 80 μM and 20 mM phosphate buffer, pH 6.0, and 310 K, and calculated using eq 5. In cases where amide-based data are not available for a non-Pro residue, the small circles placed directly underneath the sequence highlight the reason (see "H4 panel" for explanation; all correlations derived from ILV methyl groups can be analyzed). To establish the robustness of the potentials, where possible, we have calculated ϕ_{ENS} from different combinations of cosolutes. The excellent agreement between ϕ_{ENS} values calculated from measurements at the lowest (0.1 mM Gd^{+}, 2 mM Gd^{-}), intermediate (0.2 mM Gd^{+}, 4 mM Gd^{-}), and highest (0.3 mM Gd^{+}, 6 mM Gd^{-}) cosolute concentrations further establishes that binding of the compounds to the NCP is not a significant factor.

DISCUSSION

The intrinsically disordered tails of the histone components of chromatin play pivotal roles in a plethora of molecular recognition processes involving a variety of different chromatin-binding proteins,[7,8,15] in regulating both compaction and stabilization of chromatin[15,70,71,77] and in driving its

https://doi.org/10.1021/jacs.5c01567
J. Am. Chem. Soc. 2025, 147, 14519−14529

phase separation propensities.[72,73] Charge interactions make key contributions to these processes, and quantification of histone tail electrostatic potentials is therefore of importance. Here, we have used a recently developed NMR-based approach for measurement of near surface electrostatic potentials at atomic resolution, whereby paramagnetic cosolutes are added to a solution of the biomolecule of interest to enhance ^{1}H transverse spin relaxation rates in a manner that depends on the biomolecule's charge.[33] Exploiting the high relaxivities of the Gd-based cosolutes depicted in Figure 1b in relation to their nitroxide counterparts, we have performed experiments measuring sPREs of histone tail backbone amide and side chain methyl protons in a 200 kDa NCP complex, from which per-residue ϕ_{ENS} values were obtained.

Our focus here has been on the NCP tail residues exclusively. As these are surface exposed, the cosolutes can closely approach the amide or methyl probes of interest so that the interpretation of sPRE measurements in terms of near surface electrostatic potentials is straightforward. Although it would be possible to similarly measure sPRE values for the methyl probes in the core of the NCP, their interpretation, in terms of surface potentials, is more complex. As the cosolutes cannot penetrate the core, they will be at significantly further distances from most methyl probes than the corresponding tail backbone amides. Thus, a sPRE value will not report on the potential at the core methyl site per se but rather provide an average over a range of positions on the surface of the cylindrical nucleosome structure that bring the cosolute as close as possible to the methyl in question. We are currently exploring the information content in these sorts of measurements.

A strong motivation for this study was to establish whether the Lys- and Arg-rich histone tails that are positively charged in the absence of DNA retain their positive potential in the context of the NCP, or whether the effective tail charges are inverted by the negatively charged DNA in the nucleosome particle. Figure 3 shows that all per-residue ϕ_{ENS} tail values are negative, clearly establishing the influence of the DNA. To put these values into context, we have carried out a Poisson−Boltzmann calculation of ϕ_{ENS} for each residue of the isolated tails (i.e., no NCP) in an extended conformation, using the same salt concentrations as in the NMR measurements on the NCP. Average values (±1 standard deviation) of 23 ± 4 mV, 7 ± 2 mV, 22 ± 5 mV, 24 ± 6 mV, and 21 ± 3 mV were obtained for H2A N- and C-tails, H2B, H3, and H4, respectively (Figure S2). Thus, decreases in ϕ_{ENS} values of between −40 and −60 mV occur in the context of the NCP relative to the isolated tails, highlighting the large effect of the DNA on tail electrostatics.

It is well-known that ϕ_{ENS} values can be highly sensitive to salt concentration, as ions in solution screen electrostatic interactions. For example, in our previous studies of a 103 residue positively charged fragment of CAPRIN1 (pI = 11.5, net charge of +13e at physiological pH), ϕ_{ENS} values decreased by approximately 10 mV when the NaCl concentration in the buffer was raised from 0 to 50 mM.[50] As it is expected that similar changes in potentials could be observed for the highly charged NCP with salt content, it is important that salt concentrations be constant over all solutions used for the electrostatic measurements described here, recognizing that the amount of salt will vary with concentrations of both added cosolute and biomolecule. Proton pulse widths are sensitive to the ionic strength of the NMR sample and can thus be used to estimate the "effective salt concentrations" in our samples. To this end, we have prepared a calibration curve whereby the ^{1}H 90° pulse width was quantified in 20 mM phosphate buffer solutions, used in the present study, with different added concentrations of NaCl (23.5 T). From the calibrated pulse width in the sample of interest, an effective NaCl salt concentration can thus be obtained (Figure S3), corresponding to the additional amount of salt that results from adding NCP and associated ions to buffer to generate the NMR sample. On this basis, we obtain effective salt concentrations of approximately 11.2 11.6, and 15.3 mM in the diamagnetic, Gd^+ (0.2 mM), and Gd^- (4 mM) samples, respectively. In contrast, in ϕ_{ENS} tail measurements using nitroxide spin labels, the required concentrations of cosolutes are larger, and so are the effective salt concentrations in samples, especially since solubilization of the nitroxide compounds requires significant pH adjustments.[33] As excess negatively charged nitroxide cosolute is needed for the measurement of sufficiently large sPREs for the NCP, relative to the positive cosolute, a discrepancy in the salt concentration between samples can be obtained. This imbalance not only modulates electrostatic potentials in a cosolute-dependent manner but can also lead to different tail/DNA interactions, complicating the calculation of robust ϕ_{ENS} values from relaxation measurements. Notably, the NCP samples evaluated here have similar effective salt concentrations, avoiding the issues associated with the translation of sPREs to electrostatic potentials.

Figure 3 shows that although the tail potentials are all negative, there are clear distinctions between them. Based on their average ϕ_{ENS} values, the tails can be divided into two groups, corresponding to low (∼−20 mV) and high (∼−45 mV) negative potentials, comprising (H2A-N, H4) and (H2A-C, H2B, H3), respectively. We wondered whether the grouping might reflect differences in the number of charged residues in the tails or their charge densities, with more positive charge attenuating the measured surface potentials (i.e., less negative ϕ_{ENS} values). Notably, H2B and H3 tails are the most positively charged (+9e and +12e, respectively), yet these tails are highly negative in potential. Further, the charge densities for (H2A-N, H4) and for (H2A-C, H2B, H3), in units of e/residue, are (+5/11, +6/18) and (+1/6, +9/28, +12/37), respectively, taking into account the +1e charge on the terminal amino group (H2A-N, H2B, H3, and H4) and a −1e charge on the carboxy end (H2A-C), where the numerator lists the net positive charge, and the denominator is the number of amino acids for a given tail. All charge densities are between 0.17 and 0.45e/residue, and there is no clear trend linking increased positive charge density with less negative ϕ_{ENS}. Differences in potentials must reflect the interplay between the positively charged tails and the negatively charged DNA, with variations in propensities to interact with nucleosomal DNA being critical. In this regard, our data suggest that H2A-C, H2B, and H3 tails form more DNA contacts than do H2A-N and H4. Indeed, extensive molecular dynamics (MD) simulations, covering many tens of microseconds, of NCPs comprised of *Xenopus laevis* histones wrapped with human α-satellite DNA establish that H3 tails have the longest DNA residence time followed by those from H2B,[74] consistent with expectations from our electrostatics measurements, with more negative ϕ_{ENS} values reflecting, at least in part, more extensive contacts with DNA. However, predictions based on MD simulations do not always agree with

https://doi.org/10.1021/jacs.5c01567
J. Am. Chem. Soc. 2025, 147, 14519−14529

expectations based on experiment. For example, in the same study the H2A-C tails were observed to have the shortest DNA residence time in the simulations, despite the very negative ϕ_{ENS} values that we have measured. Discrepancies between simulation and experiment may reflect, in this case, differences in both DNA (147 base pair Widom-601 DNA[66] and 187 base-pair α-satellite DNA used for NMR and MD, respectively) and H2A-C histone (KTEKKA for *D. melanogaster* and KTESSKSKSK for *X. laevis*) sequences, the fact that different parameters are compared (ϕ_{ENS} vs contact lifetimes), and, most significantly, the imperfections in force fields that are used in simulations.

Notably, the two tail sequences for which low ϕ_{ENS} values (in absolute value) were measured have a high proportion of Gly residues—(4/11, 8/18) for H2A-N and H4 vs (0/6, 3/28, 4/37) for H2A-C, H2B and H3. It is of interest to note that the relative proportions of Gly residues in histone tails are very similar across many different species, from ciliates (*Paramecium caudatum*) to reptiles (*Alligator sinensis*), plants (*Arabidopsis thaliana*), *D. melanogaster*, *X. laevis*, and *Homo sapiens*, Figure S4. As the innate conformational flexibility of disordered polypeptide chains would be expected to increase with Gly content,[75] a larger entropic penalty might be accrued by restricting the conformations of Gly-enriched tails through formation of extensive contacts with nucleosomal DNA, relative to tails with fewer Gly residues. This would result in fewer interactions between Gly-rich tails and DNA, leading to less negative ϕ_{ENS} values. In this context, it is interesting to note that ^{15}N spin relaxation measurements of per-residue tail backbone dynamics establish that the H3 tail is more motionally restricted on a ps−ns time scale than H4, with H2B slightly less restricted than H3 but more so than H4.[17] Although there is no absolute correlation between decreased tail dynamics and more negative potentials, the qualitative relationships identified here do suggest that increased interactions with DNA, leading to decreased motion, influence ϕ_{ENS} values. The large potentials observed for the H2B and H3 tails may also reflect the fact that they exit the nucleosome through DNA gyres, unlike the other tails (Figure 1a), which could help position them to form more extensive DNA interactions. In particular, the lower propensities for the H4 tails to form DNA contacts could be important for favoring their interactions with acidic patches of neighboring NCPs in chromatin and, thus, in promoting DNA packing.[76]

In order to establish how electrostatic potentials of histone tails might vary for different species, we have examined a series of tail sequences, as indicated in Figure S4 and Table S1, quantifying both the charge and the fractional Gly content of each. Except for H2A-C for which the charge densities vary considerably, the remaining tails have similar charge densities and Gly contents between species, in particular H3 and H4 that are almost completely conserved. Thus, many of the tails are expected to have similar ϕ_{ENS} values to those we have measured for the *D. melanogaster* histones, at least in the context of the highly positioning Widom 601 DNA sequence.[66]

In addition to providing an exciting avenue to explore the role of electrostatics in chromatin structural dynamics and function, measurement of near surface electrostatic potentials offers an opportunity for obtaining more accurate ensembles of histone tails in NCPs than can be generated through traditional structural studies and, more generally, more representative ensembles of IDRs in other systems. This can be achieved by carrying out MD simulations with ϕ_{ENS} values as input restraints, much like how nuclear Overhauser effects, scalar and dipolar couplings, and chemical shifts are used in NMR-based analyses currently. We are pursuing this strategy along with quantifying how post-translational modifications modify such ensembles.

■ ASSOCIATED CONTENT

Supporting Information

The Supporting Information is available free of charge at https://pubs.acs.org/doi/10.1021/jacs.5c01567.

Discussion of calculation of ϕ_{ENS} values from transverse relaxation rates, details of calculation of ϕ_{PBS} values, superposition of spectra with and without 0.3 mM Gd+ cosolute, comparative potentials of isolated NCP tails and tails in the context of the intact NCP, correlation plot of the ^{1}H 90° pulse width vs NaCl concentration, sequence alignment of NCP histone tails, and charge and the fractional Gly content of tails from different species (PDF)

■ AUTHOR INFORMATION

Corresponding Authors

Nicolas Bolik-Coulon − *Department of Molecular Genetics, University of Toronto, Toronto, Ontario M5S 1A8, Canada; Department of Chemistry, University of Toronto, Toronto, Ontario M5S 3H6, Canada; Department of Biochemistry, University of Toronto, Toronto, Ontario M5S 1A8, Canada; Program in Molecular Medicine, Hospital for Sick Children Research Institute, Toronto, Ontario M5G 0A4, Canada;* orcid.org/0000-0002-2759-5767; Email: nicolas.bolikcoulon@utoronto.ca

Lewis E. Kay − *Department of Molecular Genetics, University of Toronto, Toronto, Ontario M5S 1A8, Canada; Department of Chemistry, University of Toronto, Toronto, Ontario M5S 3H6, Canada; Department of Biochemistry, University of Toronto, Toronto, Ontario M5S 1A8, Canada; Program in Molecular Medicine, Hospital for Sick Children Research Institute, Toronto, Ontario M5G 0A4, Canada;* orcid.org/0000-0002-4054-4083; Email: lewis.kay@utoronto.ca

Author

Philip Rößler − *Department of Molecular Genetics, University of Toronto, Toronto, Ontario M5S 1A8, Canada; Department of Chemistry, University of Toronto, Toronto, Ontario M5S 3H6, Canada; Department of Biochemistry, University of Toronto, Toronto, Ontario M5S 1A8, Canada; Program in Molecular Medicine, Hospital for Sick Children Research Institute, Toronto, Ontario M5G 0A4, Canada*

Complete contact information is available at: https://pubs.acs.org/10.1021/jacs.5c01567

Notes

The authors declare no competing financial interest.

■ ACKNOWLEDGMENTS

L.E.K. acknowledges support from the Canadian Institutes of Health Research (CIHR) (FND-503573) and the Natural Sciences and Engineering Council of Canada (2024-03872). N.B.-C. thanks the CIHR for a postdoctoral fellowship, and P.R. extends thanks to the Swiss National Science Foundation for financial support (Postdoc.Mobility Grant number:

214412). The authors are grateful to Professor Tae Hun Kim (Case Western Reserve University) for valuable suggestions concerning the preparation of samples and to Professor Yusuke Okuno (Washington University) for enlightening discussions.

REFERENCES

(1) Wright, P. E.; Dyson, H. J. Intrinsically Disordered Proteins in Cellular Signalling and Regulation. *Nat. Rev. Mol. Cell Biol.* **2015**, *16* (1), 18−29.
(2) Luger, K.; Mäder, A. W.; Richmond, R. K.; Sargent, D. F.; Richmond, T. J. Crystal Structure of the Nucleosome Core Particle at 2.8 Å Resolution. *Nature* **1997**, *389*, 251−260.
(3) Ghoneim, M.; Fuchs, H. A.; Musselman, C. A. Histone Tail Conformations: A Fuzzy Affair with DNA. *Trends Biochem. Sci.* **2021**, *46* (7), 564−578.
(4) Gebala, M.; Johnson, S. L.; Narlikar, G. J.; Herschlag, D. Ion Counting Demonstrates a High Electrostatic Field Generated by the Nucleosome. *Elife* **2019**, *8*, No. e44993.
(5) Lammerding, J. Mechanics of the Nucleus. In *Comprehensive Physiology*; Prakash, Y. S., Ed.; Wiley, 2011; pp 783−807..
(6) Smith, B. C.; Denu, J. M. Chemical Mechanisms of Histone Lysine and Arginine Modifications. *Biochim. Biophys. Acta, Gene Regul. Mech.* **2009**, *1789* (1), 45−57.
(7) Bannister, A. J.; Kouzarides, T. Regulation of Chromatin by Histone Modifications. *Cell Res.* **2011**, *21* (3), 381−395.
(8) Grunstein, M. Histone Acetylation in Chromatin Structure and Transcription. *Nature* **1997**, *389* (6649), 349−352.
(9) Liu, C.; Vyas, A.; Kassab, M. A.; Singh, A. K.; Yu, X. The Role of Poly ADP-Ribosylation in the First Wave of DNA Damage Response. *Nucleic Acids Res.* **2017**, *45* (14), 8129−8141.
(10) Bonfiglio, J. J.; Fontana, P.; Zhang, Q.; Colby, T.; Gibbs-Seymour, I.; Atanassov, I.; Bartlett, E.; Zaja, R.; Ahel, I.; Matic, I. Serine ADP-Ribosylation Depends on HPF1. *Mol. Cell* **2017**, *65* (5), 932−940.
(11) Jungmichel, S.; Rosenthal, F.; Altmeyer, M.; Lukas, J.; Hottiger, M. O.; Nielsen, M. L. Proteome-Wide Identification of Poly(ADP-Ribosyl)Ation Targets in Different Genotoxic Stress Responses. *Mol. Cell* **2013**, *52* (2), 272−285.
(12) Hananya, N.; Daley, S. K.; Bagert, J. D.; Muir, T. W. Synthesis of ADP-Ribosylated Histones Reveals Site-Specific Impacts on Chromatin Structure and Function. *J. Am. Chem. Soc.* **2021**, *143* (29), 10847−10852.
(13) Gibson, B. A.; Kraus, W. L. New Insights into the Molecular and Cellular Functions of Poly(ADP-Ribose) and PARPs. *Nat. Rev. Mol. Cell Biol.* **2012**, *13* (7), 411−424.
(14) Otterstrom, J.; Castells-Garcia, A.; Vicario, C.; Gomez-Garcia, P. A.; Cosma, M. P.; Lakadamyali, M. Super-Resolution Microscopy Reveals How Histone Tail Acetylation Affects DNA Compaction within Nucleosomes in Vivo. *Nucleic Acids Res.* **2019**, *47* (16), 8470−8484.
(15) Peng, Y.; Li, S.; Landsman, D.; Panchenko, A. R. Histone Tails as Signaling Antennas of Chromatin. *Curr. Opin. Struct. Biol.* **2021**, *67*, 153−160.
(16) Honig, B.; Nicholls, A. Classical Electrostatics in Biology and Chemistry. *Science* **1995**, *268* (5214), 1144−1149.
(17) Kim, T. H.; Nosella, M. L.; Bolik-Coulon, N.; Harkness, R. W.; Huang, S. K.; Kay, L. E. Correlating Histone Acetylation with Nucleosome Core Particle Dynamics and Function. *Proc. Natl. Acad. Sci. U.S.A.* **2023**, *120* (15), No. e2301063120.
(18) Nosella, M. L.; Kim, T. H.; Huang, S. K.; Harkness, R. W.; Goncalves, M.; Pan, A.; Tereshchenko, M.; Vahidi, S.; Rubinstein, J. L.; Lee, H. O.; Forman-Kay, J. D.; Kay, L. E. Poly(ADP-Ribosyl)Ation Enhances Nucleosome Dynamics and Organizes DNA Damage Repair Components within Biomolecular Condensates. *Mol. Cell* **2024**, *84* (3), 429−446.
(19) Smrt, S. T.; Gonzalez Salguero, N.; Thomas, J. K.; Zandian, M.; Poirier, M. G.; Jaroniec, C. P. Histone H3 Core Domain in Chromatin with Different DNA Linker Lengths Studied by 1H-Detected Solid-State NMR Spectroscopy. *Front. Mol. Biosci.* **2023**, *9*, 1106588.
(20) Sun, W.; Lebedenko, O. O.; Salguero, N. G.; Shannon, M. D.; Zandian, M.; Poirier, M. G.; Skrynnikov, N. R.; Jaroniec, C. P. Conformational and Interaction Landscape of Histone H4 Tails in Nucleosomes Probed by Paramagnetic NMR Spectroscopy. *J. Am. Chem. Soc.* **2023**, *145* (46), 25478−25485.
(21) Zandian, M.; Gonzalez Salguero, N.; Shannon, M. D.; Purusottam, R. N.; Theint, T.; Poirier, M. G.; Jaroniec, C. P. Conformational Dynamics of Histone H3 Tails in Chromatin. *J. Phys. Chem. Lett.* **2021**, *12* (26), 6174−6181.
(22) Zhou, B.-R.; Feng, H.; Ghirlando, R.; Kato, H.; Gruschus, J.; Bai, Y. Histone H4 K16Q Mutation, an Acetylation Mimic, Causes Structural Disorder of Its N-Terminal Basic Patch in the Nucleosome. *J. Mol. Biol.* **2012**, *421* (1), 30−37.
(23) Furukawa, A.; Wakamori, M.; Arimura, Y.; Ohtomo, H.; Tsunaka, Y.; Kurumizaka, H.; Umehara, T.; Nishimura, Y. Acetylated Histone H4 Tail Enhances Histone H3 Tail Acetylation by Altering Their Mutual Dynamics in the Nucleosome. *Proc. Natl. Acad. Sci. U.S.A.* **2020**, *117* (33), 19661−19663.
(24) van Emmerik, C. L.; van Ingen, H. Unspinning Chromatin: Revealing the Dynamic Nucleosome Landscape by NMR. *Prog. Nucl. Magn. Reson. Spectrosc.* **2019**, *110*, 1−19.
(25) Musselman, C. A.; Kutateladze, T. G. Visualizing Conformational Ensembles of the Nucleosome by NMR. *ACS Chem. Biol.* **2022**, *17* (3), 495−502.
(26) Morrison, E. A.; Bowerman, S.; Sylvers, K. L.; Wereszczynski, J.; Musselman, C. A. The Conformation of the Histone H3 Tail Inhibits Association of the BPTF PHD Finger with the Nucleosome. *Elife* **2018**, *7*, No. e31481.
(27) Shi, X.; Prasanna, C.; Soman, A.; Pervushin, K.; Nordenskiöld, L. Dynamic Networks Observed in the Nucleosome Core Particles Couple the Histone Globular Domains with DNA. *Commun. Biol.* **2020**, *3*, 639.
(28) Stützer, A.; Liokatis, S.; Kiesel, A.; Schwarzer, D.; Sprangers, R.; Söding, J.; Selenko, P.; Fischle, W. Modulations of DNA Contacts by Linker Histones and Post-Translational Modifications Determine the Mobility and Modifiability of Nucleosomal H3 Tails. *Mol. Cell* **2016**, *61* (2), 247−259.
(29) Kato, H.; Gruschus, J.; Ghirlando, R.; Tjandra, N.; Bai, Y. Characterization of the N-Terminal Tail Domain of Histone H3 in Condensed Nucleosome Arrays by Hydrogen Exchange and NMR. *J. Am. Chem. Soc.* **2009**, *131* (42), 15104−15105.
(30) McIntosh, L. P.; Naito, D.; Baturin, S. J.; Okon, M.; Joshi, M. D.; Nielsen, J. E. Dissecting Electrostatic Interactions in Bacillus Circulans Xylanase through NMR-Monitored pH Titrations. *J. Biomol. NMR* **2011**, *51* (1), 5.
(31) Hass, M. A. S.; Mulder, F. A. A. Contemporary NMR Studies of Protein Electrostatics. *Annu. Rev. Biophys.* **2015**, *44*, 53−75.
(32) Zhang, H.; Eerland, J.; Horn, V.; Schellevis, R.; van Ingen, H. Mapping the Electrostatic Potential of the Nucleosome Acidic Patch. *Sci. Rep.* **2021**, *11* (1), 23013.
(33) Yu, B.; Pletka, C. C.; Pettitt, B. M.; Iwahara, J. De Novo Determination of Near-Surface Electrostatic Potentials by NMR. *Proc. Natl. Acad. Sci. U.S.A.* **2021**, *118* (25), No. e2104020118.
(34) Yu, B.; Pletka, C. C.; Iwahara, J. Protein Electrostatics Investigated through Paramagnetic NMR for Nonpolar Groups. *J. Phys. Chem. B* **2022**, *126* (11), 2196−2202.
(35) Okuno, Y.; Szabo, A.; Clore, G. M. Quantitative Interpretation of Solvent Paramagnetic Relaxation for Probing Protein−Cosolute Interactions. *J. Am. Chem. Soc.* **2020**, *142* (18), 8281−8290.
(36) Okuno, Y.; Schwieters, C. D.; Yang, Z.; Clore, G. M. Theory and Applications of Nitroxide-Based Paramagnetic Cosolutes for Probing Intermolecular and Electrostatic Interactions on Protein Surfaces. *J. Am. Chem. Soc.* **2022**, *144* (46), 21371−21388.
(37) Chen, C.; Yu, B.; Yousefi, R.; Iwahara, J.; Pettitt, B. M. Assessment of the Components of the Electrostatic Potential of Proteins in Solution: Comparing Experiment and Theory. *J. Phys. Chem. B* **2022**, *126* (24), 4543−4554.

https://doi.org/10.1021/jacs.5c01567
J. Am. Chem. Soc. 2025, 147, 14519−14529

(38) Iwahara, J.; Pettitt, B. M.; Yu, B. Direct Measurements of Biomolecular Electrostatics through Experiments. *Curr. Opin. Struct. Biol.* **2023**, *82*, 102680.
(39) Yu, B.; Wang, X.; Tan, K. N.; Iwahara, J. Influence of an Intrinsically Disordered Region on Protein Domains Revealed by NMR-Based Electrostatic Potential Measurements. *J. Am. Chem. Soc.* **2024**, *146* (22), 14922−14926.
(40) Yu, B.; Wang, X.; Iwahara, J. Measuring Local Electrostatic Potentials Around Nucleic Acids by Paramagnetic NMR Spectroscopy. *J. Phys. Chem. Lett.* **2022**, *13* (42), 10025−10029.
(41) Toyama, Y.; Rangadurai, A. K.; Forman-Kay, J. D.; Kay, L. E. Mapping the Per-Residue Surface Electrostatic Potential of CAPRIN1 along Its Phase-Separation Trajectory. *Proc. Natl. Acad. Sci. U.S.A.* **2022**, *119* (36), No. e2210492119.
(42) Penk, A.; Danielsson, A.; Gaardløs, M.; Montag, C.; Schöler, A.; Huster, D.; Samsonov, S. A.; Künze, G. Detecting Protein-Ligand Interactions with Nitroxide Based Paramagnetic Cosolutes. *Chem.—Eur. J.* **2024**, *30* (18), No. e202303570.
(43) Morris, D. L.; Nyenhuis, D. A.; Dean, D. N.; Strub, M.-P.; Tjandra, N. Observation of pH-Dependent Residual Structure in the Pmel17 Repeat Domain and the Implication for Its Amyloid Formation. *Biochemistry* **2023**, *62* (22), 3222−3233.
(44) Baker, N. A.; Sept, D.; Joseph, S.; Holst, M. J.; McCammon, J. A. Electrostatics of Nanosystems: Application to Microtubules and the Ribosome. *Proc. Natl. Acad. Sci. U.S.A.* **2001**, *98* (18), 10037−10041.
(45) Jurrus, E.; Engel, D.; Star, K.; Monson, K.; Brandi, J.; Felberg, L. E.; Brookes, D. H.; Wilson, L.; Chen, J.; Liles, K.; Chun, M.; Li, P.; Gohara, D. W.; Dolinsky, T.; Konecny, R.; Koes, D. R.; Nielsen, J. E.; Head-Gordon, T.; Geng, W.; Krasny, R.; Wei, G.-W.; Holst, M. J.; McCammon, J. A.; Baker, N. A. Improvements to the APBS Biomolecular Solvation Software Suite. *Protein Sci.* **2018**, *27* (1), 112−128.
(46) Gilson, M. K.; Sharp, K. A.; Honig, B. H. Calculating the Electrostatic Potential of Molecules in Solution: Method and Error Assessment. *J. Comput. Chem.* **1988**, *9* (4), 327−335.
(47) Li, C.; Jia, Z.; Chakravorty, A.; Pahari, S.; Peng, Y.; Basu, S.; Koirala, M.; Panday, S. K.; Petukh, M.; Li, L.; Alexov, E. DelPhi Suite: New Developments and Review of Functionalities. *J. Comput. Chem.* **2019**, *40* (28), 2502−2508.
(48) Jiang, Y.; Yuen, R. K. C.; Jin, X.; Wang, M.; Chen, N.; Wu, X.; Ju, J.; Mei, J.; Shi, Y.; He, M.; Wang, G.; Liang, J.; Wang, Z.; Cao, D.; Carter, M. T.; Chrysler, C.; Drmic, I. E.; Howe, J. L.; Lau, L.; Marshall, C. R.; Merico, D.; Nalpathamkalam, T.; Thiruvahindrapuram, B.; Thompson, A.; Uddin, M.; Walker, S.; Luo, J.; Anagnostou, E.; Zwaigenbaum, L.; Ring, R. H.; Wang, J.; Lajonchere, C.; Wang, J.; Shih, A.; Szatmari, P.; Yang, H.; Dawson, G.; Li, Y.; Scherer, S. W. Detection of Clinically Relevant Genetic Variants in Autism Spectrum Disorder by Whole-Genome Sequencing. *Am. J. Hum. Genet.* **2013**, *93* (2), 249−263.
(49) Nakayama, K.; Ohashi, R.; Shinoda, Y.; Yamazaki, M.; Abe, M.; Fujikawa, A.; Shigenobu, S.; Futatsugi, A.; Noda, M.; Mikoshiba, K.; Furuichi, T.; Sakimura, K.; Shiina, N. RNG105/Caprin1, an RNA Granule Protein for Dendritic mRNA Localization, Is Essential for Long-Term Memory Formation. *Elife* **2017**, *6*, No. e29677.
(50) Toyama, Y.; Rangadurai, A. K.; Forman-Kay, J. D.; Kay, L. E. Surface Electrostatics Dictate RNA-Binding Protein CAPRIN1 Condensate Concentration and Hydrodynamic Properties. *J. Biol. Chem.* **2023**, *299* (1), 102776.
(51) Abramov, G.; Velyvis, A.; Rennella, E.; Wong, L. E.; Kay, L. E. A Methyl-TROSY Approach for NMR Studies of High-Molecular-Weight DNA with Application to the Nucleosome Core Particle. *Proc. Natl. Acad. Sci. U.S.A.* **2020**, *117* (23), 12836−12846.
(52) Delaglio, F.; Grzesiek, S.; Vuister, G. W.; Zhu, G.; Pfeifer, J.; Bax, A. NMRPipe: A Multidimensional Spectral Processing System Based on UNIX Pipes. *J. Biomol. NMR* **1995**, *6* (3), 277−293.
(53) Lee, W.; Tonelli, M.; Markley, J. L. NMRFAM-SPARKY: Enhanced Software for Biomolecular NMR Spectroscopy. *Bioinformatics* **2015**, *31* (8), 1325−1327.
(54) Rangadurai, A. K.; Toyama, Y.; Kay, L. E. Sometimes Pulses Just Have to Be Perfect − An Example Based on the Measurement of Amide Proton Transverse Relaxation Rates in Proteins. *J. Magn. Reson.* **2023**, *349*, 107412.
(55) Geen, H.; Freeman, R. Band-Selective Radiofrequency Pulses. *J. Magn. Reson.* **1991**, *93* (1), 93−141.
(56) Freeman, R.; Kempsell, S. P.; Levitt, M. H. Radiofrequency Pulse Sequences Which Compensate Their Own Imperfections. *J. Magn. Reson.* **1980**, *38* (3), 453−479.
(57) Tugarinov, V.; Kay, L. E. Relaxation Rates of Degenerate 1H Transitions in Methyl Groups of Proteins as Reporters of Side-Chain Dynamics. *J. Am. Chem. Soc.* **2006**, *128* (22), 7299−7308.
(58) Sklenar, V.; Piotto, M.; Leppik, R.; Saudek, V. Gradient-Tailored Water Suppression for 1H-15N HSQC Experiments Optimized to Retain Full Sensitivity. *J. Magn. Reson. A* **1993**, *102* (2), 241−245.
(59) Press, W. H.; Teukolsky, S. A.; Flannery, B. P. *Numerical Recipes in C*; Cambridge University Press.; Press Syndicate of the University of Cambridge, 2002.
(60) Yu, B.; Bolik-Coulon, N.; Rangadurai, A. K.; Kay, L. E.; Iwahara, J. Gadolinium-Based NMR Spin Relaxation Measurements of Near-Surface Electrostatic Potentials of Biomolecules. *J. Am. Chem. Soc.* **2024**, *146* (30), 20788−20801.
(61) Corsi, D. M.; Platas-Iglesias, C.; van Bekkum, H.; Peters, J. A. Determination of Paramagnetic Lanthanide(III) Concentrations from Bulk Magnetic Susceptibility Shifts in NMR Spectra. *Magn. Reson. Chem.* **2001**, *39* (11), 723−726.
(62) Peters, J. A.; Huskens, J.; Raber, D. J. Lanthanide Induced Shifts and Relaxation Rate Enhancements. *Prog. Nucl. Magn. Reson. Spectrosc.* **1996**, *28* (3), 283−350.
(63) Schrödinger, L. L. C. The PyMOL Molecular Graphics System, Version 1.8; PyMOL, 2015.
(64) Kaushik Rangadurai, A.; Toyama, Y.; Kay, L. E. Practical Considerations for the Measurement of Near-Surface Electrostatics Based on Solvent Paramagnetic Relaxation Enhancements. *J. Magn. Reson.* **2023**, *349*, 107400.
(65) Tugarinov, V.; Kay, L. E. An Isotope Labeling Strategy for Methyl TROSY Spectroscopy. *J. Biomol. NMR* **2004**, *28* (2), 165−172.
(66) Lowary, P. T.; Widom, J. New DNA Sequence Rules for High Affinity Binding to Histone Octamer and Sequence-Directed Nucleosome Positioning1. *J. Mol. Biol.* **1998**, *276* (1), 19−42.
(67) Kato, H.; van Ingen, H.; Zhou, B.-R.; Feng, H.; Bustin, M.; Kay, L. E.; Bai, Y. Architecture of the High Mobility Group Nucleosomal Protein 2-Nucleosome Complex as Revealed by Methyl-Based NMR. *Proc. Natl. Acad. Sci. U.S.A.* **2011**, *108* (30), 12283−12288.
(68) Kitevski-LeBlanc, J.; Fradet-Turcotte, A.; Kukic, P.; Wilson, M. D.; Portella, G.; Yuwen, T.; Panier, S.; Duan, S.; Canny, M. D.; van Ingen, H.; Arrowsmith, C. H.; Rubinstein, J. L.; Vendruscolo, M.; Durocher, D.; Kay, L. E. The RNF168 Paralog RNF169 Defines a New Class of Ubiquitylated Histone Reader Involved in the Response to DNA Damage. *Elife* **2017**, *6*, No. e23872.
(69) Tugarinov, V.; Hwang, P. M.; Ollerenshaw, J. E.; Kay, L. E. Cross-Correlated Relaxation Enhanced 1H−13C NMR Spectroscopy of Methyl Groups in Very High Molecular Weight Proteins and Protein Complexes. *J. Am. Chem. Soc.* **2003**, *125* (34), 10420−10428.
(70) du Preez, L. L.; Patterton, H.-G. Secondary Structures of the Core Histone N-Terminal Tails: Their Role in Regulating Chromatin Structure. In *Epigenetics: Development and Disease*; Kundu, T. K., Ed.; Springer Netherlands: Dordrecht, 2013; pp 37−55..
(71) Kan, P.-Y.; Lu, X.; Hansen, J. C.; Hayes, J. J. The H3 Tail Domain Participates in Multiple Interactions during Folding and Self-Association of Nucleosome Arrays. *Mol. Cell. Biol.* **2007**, *27* (6), 2084−2091.
(72) Sanulli, S.; Trnka, M. J.; Dharmarajan, V.; Tibble, R. W.; Pascal, B. D.; Burlingame, A. L.; Griffin, P. R.; Gross, J. D.; Narlikar, G. J. HP1 Reshapes Nucleosome Core to Promote Phase Separation of Heterochromatin. *Nature* **2019**, *575* (7782), 390−394.

(73) Gibson, B. A.; Doolittle, L. K.; Schneider, M. W. G.; Jensen, L. E.; Gamarra, N.; Henry, L.; Gerlich, D. W.; Redding, S.; Rosen, M. K. Organization of Chromatin by Intrinsic and Regulated Phase Separation. *Cell* **2019**, *179* (2), 470−484.
(74) Peng, Y.; Li, S.; Onufriev, A.; Landsman, D.; Panchenko, A. R. Binding of Regulatory Proteins to Nucleosomes Is Modulated by Dynamic Histone Tails. *Nat. Commun.* **2021**, *12* (1), 5280.
(75) Scott, K. A.; Alonso, D. O. V.; Sato, S.; Fersht, A. R.; Daggett, V. Conformational Entropy of Alanine versus Glycine in Protein Denatured States. *Proc. Natl. Acad. Sci. U.S.A.* **2007**, *104* (8), 2661−2666.
(76) Kan, P.-Y.; Caterino, T. L.; Hayes, J. J. The H4 Tail Domain Participates in Intra- and Internucleosome Interactions with Protein and DNA during Folding and Oligomerization of Nucleosome Arrays. *Mol. Cell. Biol.* **2009**, *29* (2), 538−546.
(77) Davey, C. A.; Sargent, D. F.; Luger, K.; Maeder, A. W.; Richmond, T. J. Solvent Mediated Interactions in the Structure of the Nucleosome Core Particle at 1.9 Å Resolution. *J. Mol. Biol.* **2002**, *319* (5), 1097−1113.

https://doi.org/10.1021/jacs.5c01567
J. Am. Chem. Soc. 2025, 147, 14519−14529